ACS APPLIED MATERIALS & INTERFACES
Research Article
www.acsami.org

Interface and Composition Analysis on Perovskite Solar Cells

Fabio Matteocci,[†] Yan Busby,[‡] Jean-Jacques Pireaux,[‡] Giorgio Divitini,[§] Stefania Cacovich,[§] Caterina Ducati,[§] and Aldo Di Carlo*,[†]

[†]C.H.O.S.E. (Centre for Hybrid and Organic Solar Energy), Department of Electronic Engineering, University of Rome "Tor Vergata", via del Politecnico 1, Rome 00133, Italy

[‡]Research Center in the Physics of Matter and Radiation (PMR), Laboratoire Interdisciplinaire de Spectroscopie Electronique (LISE), University of Namur, B-5000 Namur, Belgium

[§]Department of Materials Science & Metallurgy, University of Cambridge, 27 Charles Babbage road, CB3 0FS, Cambridge, U.K.

Supporting Information

ABSTRACT: Organometal halide (hybrid) perovskite solar cells have been fabricated following four different deposition procedures and investigated in order to find correlations between the solar cell characteristics/performance and their structure and composition as determined by combining depth-resolved imaging with time-of-flight secondary ion mass spectrometry (ToF-SIMS), X-ray photoelectron spectroscopy (XPS), and analytical scanning transmission electron microscopy (STEM). The interface quality is found to be strongly affected by the perovskite deposition procedure, and in particular from the environment where the conversion of the starting precursors into the final perovskite is performed (air, nitrogen, or vacuum). The conversion efficiency of the precursors into the hybrid perovskite layer is compared between the different solar cells by looking at the ToF-SIMS intensities of the characteristic molecular fragments from the perovskite and the precursor materials. Energy dispersive X-ray spectroscopy in the STEM confirms the macroscopic ToF-SIMS findings and allows elemental mapping with nanometer resolution. Clear evidence for iodine diffusion has been observed and related to the fabrication procedure.

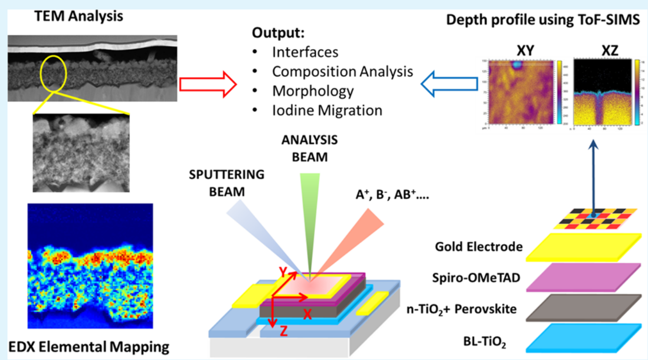

KEYWORDS: *perovskite solar cells, ToF-SIMS, XPS, EDX-STEM, filaments*

1. INTRODUCTION

Owing to their excellent optical and electric properties, organometal halide perovskites have been considered since the early 1990s as possible materials for solution-processed optoelectronic devices.[1] However, only recently have perovskites gained worldwide interest due to breakthrough performance when used in photovoltaic devices. In the past few years, perovskite-based solar cell (PSCs) have shown a rapid increase in their power conversion efficiency (PCE) going from 3.8%[2] to 20.1%[3] on small area devices and reaching a PCE of 13% and 9.3% on modules with active areas of 10 and 100 cm^2, respectively.[4,5] Thus, hybrid perovskites represent a promising alternative class of light harvesters for thin film photovoltaic devices in terms of cost and processability with respect to more established competitors, such as CdTe, CIGS, and a-Si.

A critical issue for PSCs is related to their long-term device stability. Moisture has been demonstrated to play a major role in degrading long-term performance of PSCs.[6] The effect of moisture can be alleviated by modifying the perovskite composition by doping with Br atoms,[7] by modifying the device architecture by inserting an alumina layer between the perovskite and the hole-transport material (HTM),[8,9] or by varying the environment where the conversion of the precursors into the perovskite structure (perovskite conversion) takes place.[10] Nevertheless, an efficient sealing strategy is mandatory to avoid in-service penetration of the moisture into the cell.[11,12] Several studies have been devoted to obtain high-quality perovskite films by increasing the perovskite coverage,[13] and by optimizing perovskite crystal size.[14] This perovskite layer optimization has led to the identification of efficient solution-based perovskite deposition methods leading to high PCE solar cells: these are commonly referred to as the two-step deposition,[13] one-step deposition with chlorine doping,[15,16] vapor assisted solution deposition (VASP),[17,18] and solvent engineering method.[19]

PSCs are heterogeneous systems comprising multiple layers of materials characterized by very different morphologies and physical/chemical characteristics. The device performance is well-known to critically depend on the interfaces between the layers; it was shown that different processing conditions of the same starting precursors result in a high variability of performance.[20]

Received: September 1, 2015
Accepted: November 2, 2015
Published: November 2, 2015

DOI: 10.1021/acsami.5b08038
ACS Appl. Mater. Interfaces 2015, 7, 26176−26183

Table 1. Deposition Methods and Conditions for Each Sample Studied in This Work

sample	method	perovskite precursor	layer deposition	conversion process	conversion environment
A	two-step	PbI_2 (400 mg/mL)	spin-coating	VASP (90 min)	vacuum
B	two-step	PbI_2 (460 mg/mL)	spin-coating	MAI dip (10 min)	N_2
C	two-step	PbI_2 (330 mg/mL)	blade-coating	MAI dip (30 min)	air
D	one-step	$PbCl_2$+ MAI (35% in weight)	spin-coating	heat 90° (60 min)	N_2

In this paper, we investigate the structural and interfacial properties of PSCs fabricated with different methods in order to correlate the deposition technique to the electro-optical device features and their structural, compositional, and interface characteristics. PSCs deposited following four different fabrication routes have been tested and compared. The perovskite deposition methods include two-step deposition with perovskite conversion in vacuum (sample labeled "A"), in controlled nitrogen atmosphere ("B"), or in air ("C") and a one-step process with lead chloride precursor carried out in a nitrogen-filled glovebox ("D"). Sample C was realized optimizing the deposition of the lead iodide using air-assisted blade coating technique as reported in a previous work.[5] The device structure has been analyzed with scanning transmission electron microscopy (S/TEM), the atomic composition with high resolution energy-dispersive X-ray spectroscopy (EDX) and X-ray photoelectron spectroscopy (XPS), the interfaces and molecular analysis have been performed with time-of-flight secondary ion mass spectrometry (ToF-SIMS) with 3D imaging capability. Moreover, the molecular analysis is used to evaluate and compare the perovskite conversion efficiency associated with each deposition method. The combination of complementary techniques allows a full characterization of the materials which well correlates with the PSC performance.

2. RESULTS AND DISCUSSION

2.1. Electrical Characterization of the Solar Cells. The deposition procedure and conditions for each sample are summarized in Table 1. The perovskite layer deposition (method and precursor solution) and the perovskite conversion process (environment, thermal annealing) were optimized according to previous results.[4,5,15,18] Current−voltage characteristics under 1 SUN illumination are displayed in Figure 1, while the main photovoltaic parameters are reported in Table 2. Sample B (2-step, conversion in glovebox) showed the best

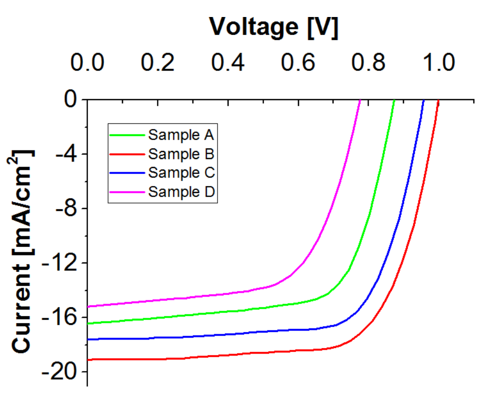

Figure 1. Current−voltage characteristics (reverse scan, scan speed 0.15 V/s) of the PSCs described in the Experimental Section. The devices were measured under Class A sun simulator (SUNABET2000, Xenon Lamp) at 1 SUN illumination conditions. The solar cells parameters and efficiency are reported in Table 2.

Table 2. Current−Voltage Characteristics of the Various PSC Samples Described in the Experimental Section

sample	V_{OC} [mV]	J_{SC} [mA/cm^2]	FF (%)	efficiency [%]
A	872	−16.36	68.1	9.7
B	998	−18.83	70.6	13.3
C	956	−17.47	71.3	11.9
D	775	−15.17	63.2	7.4

performance, reaching a PCE of 13.3% with high V_{OC} (998 mV) and J_{SC} (18.8 mA/cm^2). Interestingly, sample C (2-step, conversion in air) showed similarly high PCE of 11.9%, demonstrating that the (short-term) performance is not strongly affected by the perovskite conversion environment. Furthermore, sample A (2-step, conversion in vacuum) shows the lowest V_{OC} within the devices deposited with a double step, yielding a lower PCE of 9.7%. This result could be ascribed to the uncompleted perovskite conversion within the mesoporous TiO_2 layer and/or to the presence of thinner and nonuniform perovskite layer (as will be shown in cross-sectional TEM images reported later in this paper). Although the presence of a thick and uniform perovskite capping layer between the HTM and the TiO_2 (as obtained on the samples B and C) is beneficial in efficiently preventing charge recombination, the decrease in the V_{OC} observed in the VASP deposited perovskite suggests intrinsic issues limiting the perovskite formation into the mesoporous TiO_2. In the literature, higher PCE values have been obtained with VASP technique only on planar structure devices.[18] A strong reduction in the J_{SC} is observed in sample D (1-step, conversion in glovebox) which also displays a fairly low V_{OC} value and a lower PCE compared to devices processed with a double-step method. In the literature such behavior has been ascribed to a possible discontinuous perovskite layer leading to a direct contact between the HTM and the mesoporous TiO_2 scaffold.[21,22] Furthermore, the analysis of the hysteresis effect on $J-V$ characteristics is included in the Supporting Information. The hysteresis behavior is compared by calculating an hysteresis index (h_i) defined as the ratio between the PCE measured in reverse (PCE_{REV}) and forward scan (PCE_{FOR}) directions. Sample A and C show lower hysteresis indices (h_A = 1.0898 and h_C = 1.0917); the higher hysteresis measured in sample B (h_B = 1.170) is possibly ascribed due to the larger perovskite crystals size.[14] The hysteresis effect in the sample D is negligible (h_D = 1.0137). To provide full information on the characterization of the devices, incident photon to converted electron (IPCE) and UV−vis absorbance spectra have been measured for each sample (see Figure S2 and S3 in the Supporting Information).

2.2. Structural and Composition Analysis (STEM/EDX/XPS). Samples were prepared into lamellae for STEM-EDX analysis using focused ion beam (FIB) milling. The extracted volume that can be investigated with high spatial resolution is roughly 5 μm wide and 150 nm thick; the sampling area that can be obtained is thus considerably smaller than the one analyzed using XPS or TOF-SIMS that will be presented later.

DOI: 10.1021/acsami.5b08038
ACS Appl. Mater. Interfaces 2015, 7, 26176−26183

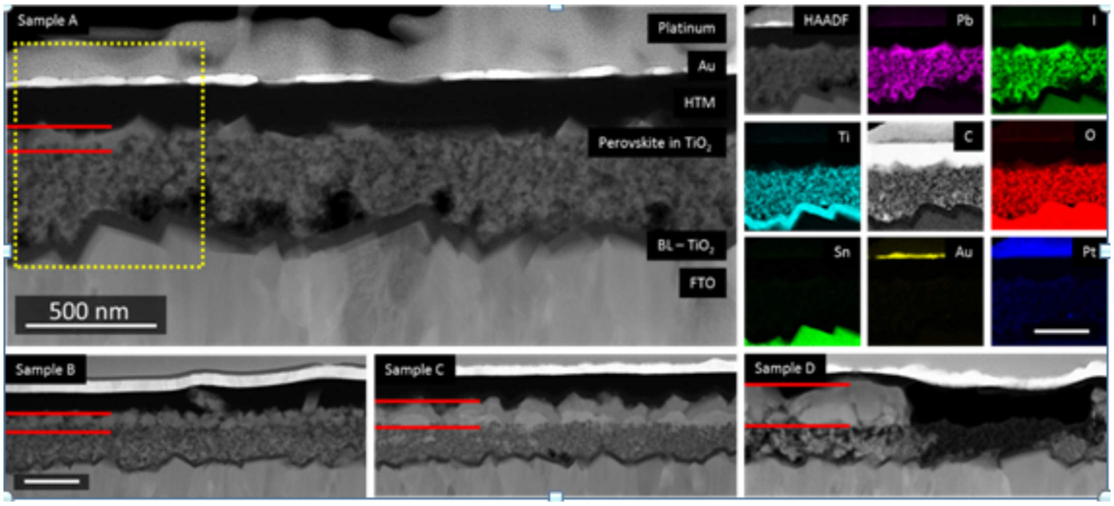

Figure 2. High angle annular dark field scanning transmission electron micrographs showing cross-sectional views of the different samples. Incomplete perovskite infiltration can be seen in samples A and D. The perovskite capping layer (sometimes discontinuous) is highlighted by red lines. (Top right) EDX maps showing the elemental distribution for the area in the dashed rectangle in sample A. All scale bars are 500 nm.

Morphologies of the different samples are shown in Figure 2, where the different layers are labeled. The morphology of the different samples is consistent with scanning electron micrographs reported by other groups.[23,24] The images represent the STEM-HAADF (high angle annular dark field) signal, which is proportional to the thickness—roughly homogeneous in these cases—and to the average atomic number; gold appears very bright, while titania, carbon, and voids look dark. The platinum coating that can be seen in the figure is deposited as a protective buffer during FIB preparation. The main differences in the morphology of the samples concern the degree of infiltration of the perovskite inside the mesoporous TiO_2 and the structure of the capping perovskite layer. Whereas samples B and C display a good infiltration of lead and iodine in the mesoporous TiO_2, samples A and D contain regions of low density, visible as dark areas in the HAADF images where the infiltration was incomplete. In sample A such regions are located at the interface between the mesoporous scaffold and the compact TiO_2 layers, while in sample D a considerable portion of the scaffold is not infiltrated. This poor pore filling fraction of the perovskite into the TiO_2 layer suggests that the single-step conversion dynamics occur before full infiltration is achieved, preventing full diffusion of the precursors. Additional XPS characterization of sample D will be discussed later in this section. The capping perovskite layers are also different in thickness and grain size. Sample B, which has the highest PCE, contains evenly distributed grains with a size of around 100 nm. Sample A presents a much thinner and patchy capping perovskite layer, while sample C shows large crystals (200–300 nm), resulting in a much rougher surface. This can be ascribed to the use of the air-flow during the lead iodide deposition using blade coating technique.[5] Moreover, the capping perovskite layer in sample C shows two different intensity levels, suggesting that the crystal size in the depth direction is larger than the lamella thickness (~150 nm), as observed in the literature.[24] The analysis of elemental distributions corroborates the STEM-HAADF information on infiltration, as can be seen in the maps in Figure 2. Interestingly, in sample C, Pb and I maps (Figure 3) show iodine diffusion in the top HTM layer. This is suspected to be one of the main pathways of cell performance degradation and is here observed for the first time with nanometer-scale spatial resolution. The migration is not observed to the same extent in the EDX maps on other samples.

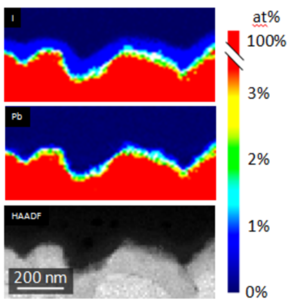

Figure 3. STEM-HAADF image and EDX maps for lead and iodine for sample C. Contrast has been enhanced to display low concentrations at the perovskite/HTM interface. Iodine presence into the HTM layer is clearly visible.

The perovskite distribution in sample D is very nonuniform, with large gaps (~1 μm) in the capping film and grains up to ~500 nm in size. This indeed explains the lower photoinduced current levels measured for sample D: the effective volume of the cell is smaller than the nominal value, and the optical density of the cell is inhomogeneous.

In order to gain more quantitative information we have performed depth profile analysis with XPS on sample D. In Figure 4 the in-depth distribution of the atomic species percentages are shown as a function of the sputtering time. The XPS analysis allows quantification of gold diffusion associated with the top contact deposition, which is found to be ~0.5% at the top of the perovskite layer (etch time ~2000 s) and ~0.1% at the bottom of the perovskite layer (etch time ~3000 s). When the profile is at the interpenetrating region between the perovskite and the mesoporous TiO_2 (etch time between 3000 and 5000 s) the Pb and I at % drops to roughly half of their value in the capping perovskite layer. Interestingly, the I/Pb ratio is about 1.4 in the capping perovskite layer (consistent with EDX STEM quantification), whereas it is close to 2 within the TiO_2 scaffold. The presence of regions of constant Pb/I ratio is an indication that in our conditions preferential sputtering does not significantly affect the I/Pb value.

DOI: 10.1021/acsami.5b08038
ACS Appl. Mater. Interfaces 2015, 7, 26176−26183

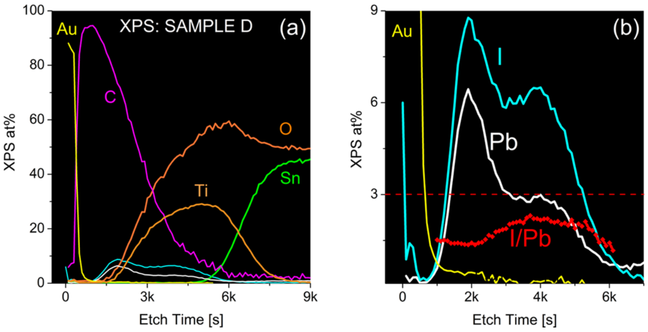

Figure 4. XPS depth profile on sample D. Percentages of the atomic species are evaluated from the survey spectra acquired at each profile step. (a) The atomic percent of gold (Au), oxygen (O), lead (Pb), titanium (Ti), tin (Sn), and carbon (C) are shown. (b) Closer look to the atomic percent of Pb and I. The I/Pb ratio is shown by the red dotted line, and the theoretical value in the perovskite is indicated by the dashed red line.

Interestingly, the I/Pb ratio is always lower than the theoretical value of 3. As it will be clarified by the ToF-SIMS analysis, this difference is thought to rely on the presence of "free" iodine and precursor elements not converted into the perovskite material (such as PbI, PbI_2, ...). The iodine at % at the gold surface reaches 6% which testifies that remarkable iodine diffusion takes place through the gold electrode. In XPS quantification Pb and I atoms in any form are (equivalently) counted in the atomic percentage value; the conversion efficiency of the perovskite is thus not accessible through this analysis. For this reason, XPS depth profiling was limited to sample D. In the following sections molecular investigations aimed to identify the exact composition of the perovskite layer were performed with ToF-SIMS.

2.3. Interface Analysis Using ToF-SIMS Depth Profile and 3D Imaging. Dual beam ToF-SIMS depth profiling is performed to reveal the distribution of constituent elements and possibly relate it to the perovskite deposition process and the solar cell performance. In order to compare the signal intensities in the different profiles, the intensities have been calibrated so that the Au_3^- counts measured on the top electrode are the same. The sputtering is operated with the low energy (500 eV) Cs^+ beam which has the advantage of providing similar etch rates on organic and inorganic materials thanks to the synergy between mechanical and chemical erosion processes taking place on the surface.[25] ToF-SIMS profiles of sample A, B, C, and D are reported in Figure 5. The most pertinent molecular fragments have been selected to identify the different interfaces. Au_3^- is selected for identifying the gold electrode, C_2N^- for the Spiro-OMeTAD, $Pb_2I_3^-$ for the perovskite, $^{37}Cl^-$ for the chlorine, O_2^- for oxygen, and TiO_3^- for the TiO_2. By comparing the profiles from samples deposited with a two-step deposition process, we immediately see that the interface quality is strongly affected by the perovskite conversion environment. The profile of sample A (Figure 2a) is the one displaying the sharpest interfaces, with a marked drop of the signals from the perovskite ($Pb_2I_3^-$) at the interface with the mesoporous TiO_2 layer marked by the raise of TiO_3^- signal (the interface with compact TiO_2 layer can be identified in the profiles by the change of the slope of the TiO_3^- and I_2^- signals). In sample B, C and D (Figure 5b−d) we observe a higher diffusion of gold and iodine and a much broader interpenetration region between the perovskite and the mesoporous TiO_2. Oxygen mostly comes from the TiO_2,

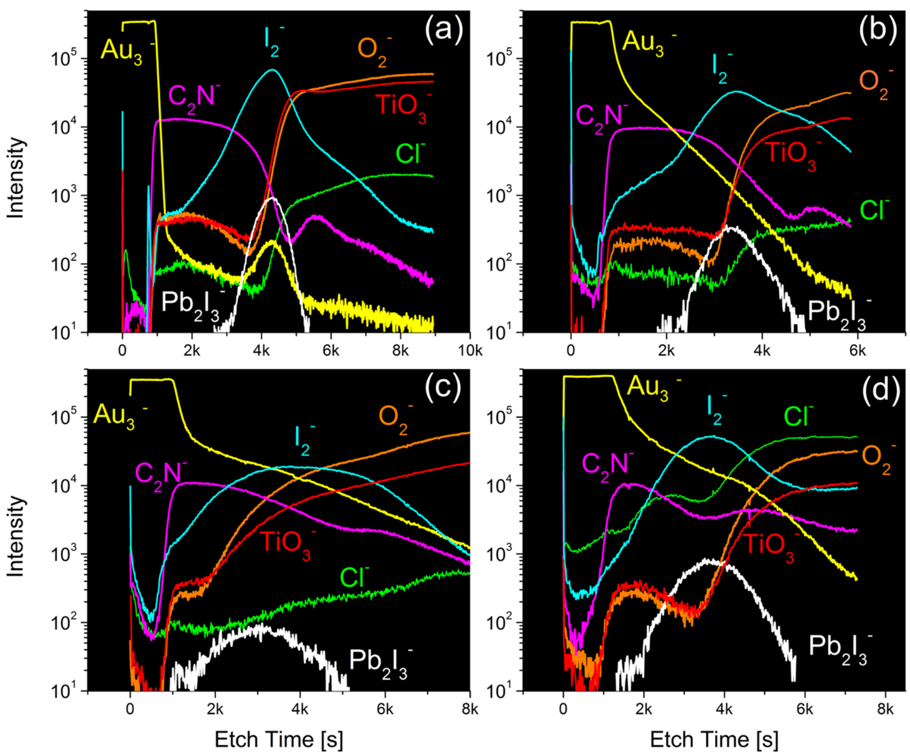

Figure 5. ToF-SIMS depth profiles of the samples A (a), B (b), C (c), and D (d). The molecular fragments from the gold top electrode (Au_3^-, at 590.9 amu), the Spiro-OMETAD (C_2N^-, at 37.0 amu), the perovskite ($Pb_2I_3^-$, at 796.6 amu), iodine (I_2^- at 253.8), and the TiO_2 (O_2^-, at 32.0 amu) are shown. Chlorine diffusion is also monitored ($^{37}Cl^-$ isotope).

DOI: 10.1021/acsami.5b08038
ACS Appl. Mater. Interfaces 2015, 7, 26176−26183

however, in sample C, due to the air conversion, the O_2^- intensity in the perovskite layer is twice as high as the TiO_3^- intensity (while it is comparable in other samples). The interfaces are much broader in sample C in agreement with the higher interface roughness determined by STEM. The O_2^- intensity has a relative maximum in the spiro-OMeTAD top surface due to the p-doping process, which is done by exposing the layer to air for 4 h prior to the back-contact deposition.[26] Chlorine distribution has been carefully monitored especially in sample D (Figure 5d). Chlorine contamination is typically observed in the ToF-SIMS profiles because of its high ionization yield, however, in sample D up to 100 times higher chlorine signal intensity (compared to samples A, B, and C for which chlorine is only due to contamination from air exposure or solvent residues) is measured in the underlying mesoporous TiO_2 layer. This is indeed a clear indication of chlorine diffusion; however, according with recent studies,[27,28] chlorine signal was not detectable in XPS meaning that its associated atomic percentage is below the detection limit of 0.1%.

Further investigation has been carried with ToF-SIMS 3D analysis. In particular, metal diffusion has been carefully investigated since inhomogeneous metal diffusion has been recently shown to possibly lead to the formation of filaments in hybrid electronic device.[29,30] In Figure 6 the ToF-SIMS 3D analysis on sample A is reported. Figure 6a shows the 150 × 150 μm^2 Au_3^- *XY* map. The inhomogeneous gold distribution is testified by the presence of few microns sized spots (as in R1 region) where a localized gold diffusion occurs into the underlying layers. 2D Maps are generated by integrating the gold signal from the 2D images acquired at each profile step. The Au_3^- profile reconstruction in the regions R1 and R2 (Figure 6b), allows comparing the gold signal intensity as a function of the depth (sputtering time). In R2, the gold signal drops sharply at the Au/Spiro-OMeTAD interface while in R1 it persists through the entire device depth. This is visually shown in the cross section reconstruction along *YZ* direction in Figure 6c. It is important to stress the fact that the Au_3^- intensity in Sipro-OMeTAD layer is at least 200 times lower on the top electrode, and it further decreases exponentially with the depth. This is an indication of a weak gold diffusion, however, by exposing the device to bias ranges higher than conventional ones, conductive metal filaments could be possibly generated by field enhanced diffusion.[29] Inhomogeneous gold diffusion can occur by diffusion through pinholes in the organic HTM or, as shown in the *XZ* cross section reconstruction in Figure 6d it can occur in coincidence of structural defects which propagates from the mesoporous TiO_2 layer and finally induce cracks in the perovskite layer. Structural defects (holes) in the TiO_2 could originate from the presence ethyl-cellulose agglomerates in the TiO_2 paste used in the in the screen-printing process. In Sample B, C, and D, while the mean gold diffusion is higher (according to ToF-SIMS profiles), we could not identify such spots in the Au_3^- *XY* maps. This has to be ascribed to the higher ability of the dipping based techniques to fill the TiO_2 defects and possibly to the higher HTM/Perovskite interface roughness leading to a lower channeling of the evaporated metal leading to a more uniform gold diffusion at the micron scale.

2.4. Perovskite Conversion Efficiency. Composition analysis with EDX, XPS, and ToF-SIMS have revealed iodine diffusion leading to an inhomogeneous lead/iodine ratio, with marked composition differences between in the capping perovskite layer and the one embedded into the mesoporous TiO_2 layer. It is then crucial to establish whether the constituent elements of the perovskite are present in the desired perovskite form (i.e., $CH_3NH_3PbI_3$) or in other forms (PbI_3 or PbI_2, etc.) as this would allow to compare the perovskite conversion efficiency associated with the each conversion method and environment and determine ionic diffusion testified by the presence of strong signals from iodine fragments. To do this, we selected from the ToF-SIMS profiles the most characteristic fragment from the crystallized perovskite ($Pb_2I_3^-$, which is totally absent outside the perovskite layer) and a second fragment PbI_3^- which has the strongest intensity in the perovskite layer, but it is thought to be found also where iodine and lead are bound to form isolated PbI_3 (i.e., not converted into the perovskite structure). The profiles obtained in each sample together with the ratio between PbI_3^- and the (smoothed) $Pb_2I_3^-$ signals (named R_i) are displayed in Figure 7. In a homogeneous perovskite layer R_i would be constant; an increase in R_i is an indication of higher abundance of PbI_3 not in the perovskite form. In sample D (single step, Figure 7d), PbI_3 signal displays a remarkable raise in the mesoporous TiO_2 matrix indicating a possible iodine diffusion

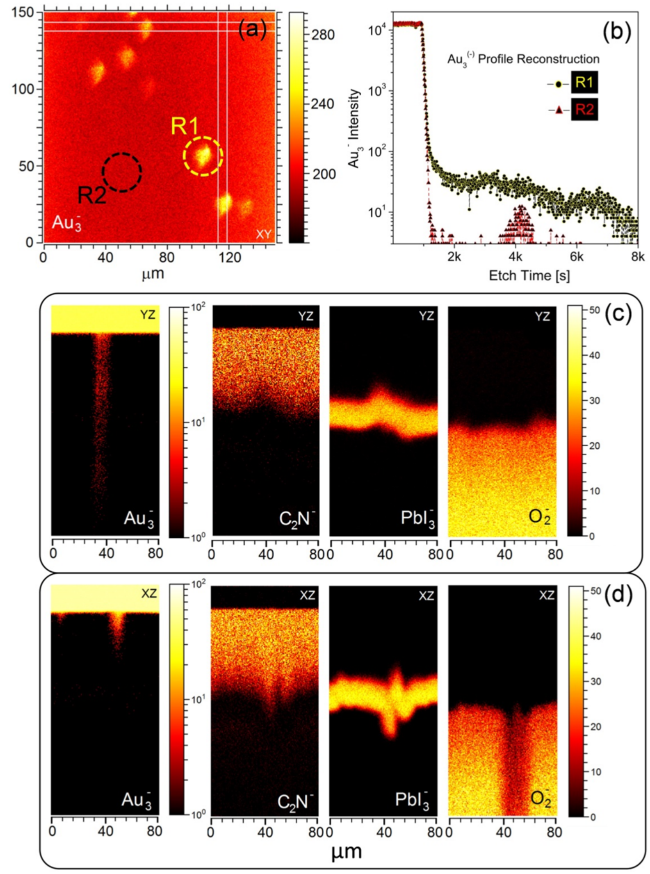

Figure 6. ToF-SIMS 3D analysis on sample A. (a) Au_3^- *XY* map showing the top electrode signal integrated over the entire profile depth. The Au_3^- profile in the regions R1 and R2 is reconstructed in panel b. In the spot region (R1) the gold signal persists through the entire device depth. This is visually confirmed by the cross section reconstructions along *YZ* (c) and *XZ* (d) directions (indicated in panel a by the parallel white lines) by displaying the characteristic molecular fragments from the Spiro-OMETAD (C_2N^-), the perovskite (PbI_3^-), and the TiO_2 (O_2^-) layers. In panel d, a defect in the TiO_2 layer propagates to the overlying layers and finally induces a local inhomogeneous gold distribution.

DOI: 10.1021/acsami.5b08038
ACS Appl. Mater. Interfaces 2015, 7, 26176−26183

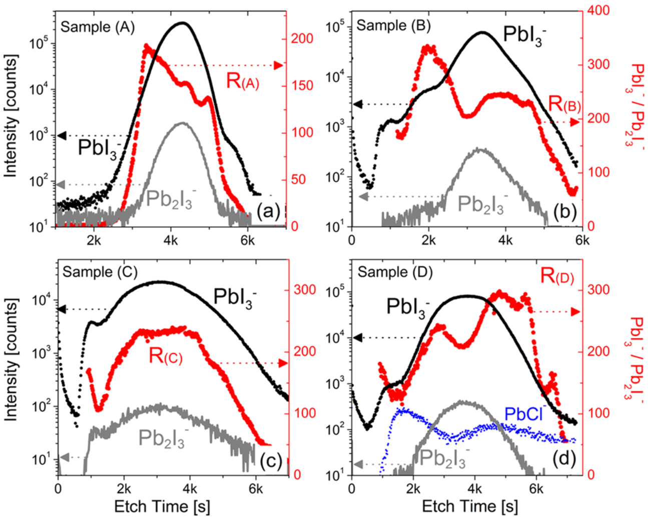

Figure 7. Tof-SIMS depth profiles of sample A (a), B (b), C (c), and D (d) described in Table 1, showing the in-depth distribution of $Pb_2I_3^-$, PbI_3^- (black and gray curves, left *Y*-scale), and the ratio PbI_3^-/$Pb_2I_3^-$ ($R_{A,B,C,D}$, right *Y*-scale). The $Pb_2I_3^-$ fragment is a characteristic from the formed perovskite while PbI_3^- is thought to be found (also) where the Pb and I are not converted into the perovskite structure.

into the TiO_2 scaffold not efficiently forming the perovskite structure (in agreement with STEM results). This would contribute to the lower PCE value of the one-step processed sample. The signal from $PbCl^-$ is found to be very low and fairly constant, indicating that the $PbCl_2$ precursor is almost absent. In sample A (Figure 7a), the perovskite layer is very compact, The strong decrease in R_A within the perovskite layer indicates that the perovskite formation is inhomogeneous with a more efficient conversion at the bottom part of the perovskite layer, while more Pb_XI_Y species are present at the interface with the HTM not bound into the perovskite structure. In sample B, R_B is fairly stable within the perovskite layer, indicating an efficient and homogeneous perovskite conversion which well fits with the high PCE values. The raise of R_B indicated some iodine diffusion toward the HTM. In sample C, similarly to sample B, R_C displays a constant value in the perovskite layer.

3. CONCLUSIONS

This work has explored in detail the morphology, composition, and interfaces in PSCs deposited by different methodologies and external conditions by combining multiple advanced characterization tools. In particular, the single-step and double-step deposition routes have been investigated. By STEM analysis, in the double-step deposition procedure the perovskite crystallization environment was found to strongly affect the perovskite domains size and the interface quality. Vacuum processing (VASP) has been found to lead to more compact layers with well-defined interfaces as confirmed by all our characterizations. By ToF-SIMS imaging defects in the underlying layers are found to possibly induce cracks in the perovskite and allow the percolation of the evaporated metal from the top electrode. Moreover, SEM/EDX analysis revealed that the perovskite layer deposited by VASP is inhomogeneous and does not fully infiltrate the mesoporous TiO_2 layer, leading to a lower PCE value. The two step conversion in liquid leads to the highest PCE value due to a homogeneous composition in both the capping perovskite and the mesoporous TiO_2 layer. The air conversion leads to much rougher interfaces, larger perovskite crystal domains, and a possibly higher iodine diffusion toward the HTM layer. Interestingly, the higher oxygen signal measured in the ToF-SIMS profiles of the perovskite formed in air is not associated with a sensibly lower efficiency of the solar cell. Conversely, the efficiency appears to be more strongly related to the quality of the interpenetration region between perovskite and mesoporous TiO_2. This is confirmed by the analysis on the one-step method sample, displaying the lowest PCE value, and for which even if the HTM/perovskite interface is sharp and low iodine diffusion occurs, the pore filling of the mesoporous TiO_2 layer is highly inhomogeneous leading to a lower coverage and a lower perovskite formation efficiency as evaluated from STEM-EDX and ToF-SIMS analyses, respectively.

4. EXPERIMENTAL SECTION

4.1. Device Fabrication. *4.1.1. Common Deposition Steps.* A raster scanning laser (Nd:YVO_4 pulsed at 30 kHz average output power $P = 10$ W) is used to etch the FTO/glass substrates (Pilkington, 8 Ω cm^{-1}, 25 mm × 25 mm). The patterned substrates are cleaned in an ultrasonic bath, using detergent with deionized water, acetone and isopropanol (10 min for each step). A 80 nm-thick patterned blocking TiO_2 layer (BL-TiO_2) is then deposited on the patterned FTO using Spray Pyrolysis Deposition according to previously reported procedure.[31] A 250 nm-thick mesoporous TiO_2 layer (18NR-T paste, Dyesol, diluted with terpineol and ethylcellulose) is deposited by screen-printing over the BL-TiO_2 surface and sintered at 480 °C for 30 min. The final thickness is measured by profilometer (Veeco 150, Dektak). The perovskite layer deposition is performed following four different approaches, which are discussed below. The hole transport material (HTM) is then deposited by spin-coating a 75 mg mL^{-1} solution of 2,20,7,70-tetrakis(*N*,*N*-dip-methoxyphenylamine)9,9′-spirobifluorene (Spiro-OMeTAD) doped with 8 μL of *tert*-butylpyridine and 12 μL of lithium bis(trifluoromethanesulfonyl)imide (Li-TFSI) solution (520 mg in 1 mL of acetonitrile). After 4 h of air exposure, the samples are transferred into a high vacuum chamber (10^{-6} mbar) to thermally evaporate a 100 nm thick Au top contact. The active area of each cell is 0.5 cm^2, calculated as the overlap area between the top and the bottom electrode. Masked devices are tested using an aperture of 0.25 cm^2 under solar simulator (class A) at AM 1.5 G and 100 mW cm^{-2} illumination conditions, calibrated with a Skye SKS 1110 sensor. Samples are then glass−glass encapsulated with a thermoplastic gasket[12] to protect the perovskite layer from moisture before the characterization steps. Incident photon-to-current conversion efficiency (IPCE) was measured for all samples using an apparatus made of an amperometer (Keithley 2612) and a monochromator (Newport Mod. 74000). UV−vis spectra were measured with a Shimadzu UV-2550 (PC)/MPC 2200 spectrophotometer using an integrating sphere.

4.1.2. Perovskite Layer Deposition. The perovskite layer is deposited following a two-step method in samples A, B, and C, and a one-step process in sample D. The deposition conditions, such as the PbI_2 concentration and the conversion time, have been optimized based on our previous results.[4,5,12,18]

Sample A. First, PbI_2 powder (Aldrich, 99%) is dissolved in dimethylformamide (DMF) with a concentration of 400 mg mL^{-1} and stirred at 70 °C. The hot PbI_2 solution is spin-coated on the mesoporous TiO_2 scaffold at 4000 rpm for 30 s on substrates preheated at 70 °C. The sample is successively dried at 120 °C for 1 h in air to remove the solvent and drive the crystallization. The second step of the procedure, corresponding to the perovskite conversion, is performed by VASP in low vacuum (0.02 mbar): the sample is put on a hot plate (150 °C) surrounded by methylammonium iodide (MAI) powder for 90 min.

Sample B. Lead iodide solution (PbI_2 in *N*,*N*-dimethylformamide, 460 mg mL^{-1}) is spin-coated at 6000 rpm for 10 s and then dried at 70 °C for 60 min. The perovskite conversion ($CH_3NH_3PbI_3$ crystallization) is operated in glovebox filled with nitrogen by dipping the

DOI: 10.1021/acsami.5b08038
ACS Appl. Mater. Interfaces 2015, 7, 26176−26183

PbI_2 layer in MAI solution (CH_3NH_3I in anhydrous isopropanol 10 mg mL^{-1}, Dyesol) for 10 min and then washing with anhydrous isopropyl alcohol, dried at 5000 rpm for 30 s, and then heated at 70 °C for 30 min.

Sample C. Lead iodide solution (PbI_2 in *N*,*N*-dimethylformamide, 330 mg mL^{-1}) is deposited by a blade-coating technique; the blade is set to a height of 100 μm above the sample surface driven at a speed of 40 mm s^{-1}. To obtain a compact and smooth layer, an air flow (speed 17 m^3 s^{-1}, temperature 100 °C) is used to quickly evaporate the solvent after the deposition. The perovskite conversion is operated in air by dipping in MAI solution (10 mg mL^{-1} in anhydrous isopropyl alcohol) for 30 min. Then the sample is washed with isopropyl alcohol, dried with nitrogen flow, and then heated at 70 °C for 30 min.

Sample D. MAI solution and $PbCl_2$ powder (98%, Sigma-Aldrich) are mixed without further purification (3:1 mass ratio) and dissolved in DMF (40% w/w). The solution is then spin-coated in a glovebox filled with nitrogen at 2000 rpm for 60 s. The perovskite conversion is performed by heating the sample at 90 °C for 60 min.

4.2. Solar Cell Characterizations. ToF-SIMS 3D chemical analysis is carried with a dual beam TOF-SIMS IV (IONTOF) spectrometer equipped with a 25 keV Bi_3^+ beam for the analysis and a 500 eV Cs^+ ion beam for the sputtering operated in noninterlaced mode. These conditions allow for an in-plane resolution of about 1 μm, an in-depth resolution of about 1 nm and a mass resolution of $M/\Delta M \sim 5000$. XPS depth profiles (ESCALAB 250Xi,Thermo Scientific) are built by successively alternating 100 s sputtering with 1 keV Ar^+ beam and XPS analysis performed with a monochromatic Al Kα X-ray beam with a spot size of 300 μm. Quantification is evaluated after Shirley background subtraction with Avantage software on survey spectra acquired at 150 eV pass energy. Sealed cells were opened just before the analyses.

Samples for TEM were prepared in a FEI Helios Nanolab FIB/SEM as a lamella using a conventional procedure.[32] Sealed cells were opened just before FIB processing (occurring in high vacuum) and, after preparation into a lamella, the samples were immediately transferred (in air) for TEM analysis, limiting overall exposure to the environment to about 10 min. STEM/EDX was carried out in a FEI Osiris (200 kV acceleration voltage) equipped with a X-FEG gun and a Bruker Super-X EDX detector. EDX maps were acquired over an area of ~1 μm^2 (with small variations due to the active layer thickness in the different samples) with a pixel size of 10 nm and a dwell time of 100 ms per pixel, using a beam current of 700 pA. Repeated STEM imaging and EDX maps acquisition were carried out to check for beam-induced degradation of the region of interest, finding the samples stable under such conditions for the duration of the experiment.

■ ASSOCIATED CONTENT

Ⓢ Supporting Information

The Supporting Information is available free of charge on the ACS Publications website at DOI: 10.1021/acsami.5b08038.

> Figure S1: Hysteresis measurements. Figure S2: Incident photon to converted electron spectra of the measured cells. Figure S3: UV−vis absorption spectra. Figure S4: XPS survey spectra (PDF)

■ AUTHOR INFORMATION

Corresponding Author

*E-mail: aldo.dicarlo@uniroma2.it.

Notes

The authors declare no competing financial interest.

■ ACKNOWLEDGMENTS

We acknowledge Lucio Cinà, Simone Casaluci, Stefano Razza, and Narges Yaghoobi Nia for the technical support, and "Polo Solare Organico" Regione Lazio, the "DSSCX" MIUR-PRIN2010 and FP7 ITN "Destiny" for funds. G.D., S.C., and C.D. acknowledge funding from ERC under grant number 259619 PHOTO EM. C.D. acknowledges financial support from the EU under grant number 312483 ESTEEM2. F.M. and Y.B. contributed equally to this work.

■ REFERENCES

(1) Mitzi, D. B.; Wang, S.; Feild, C. A.; Chess, C. A.; Guloy, A. M. Conducting Layered Organic-inorganic Halides Containing <110>-Oriented Perovskite Sheets. *Science* **1995**, *267*, 1473−1476.

(2) Kojima, A.; Teshima, K.; Shirai, Y.; Miyasaka, T. Organometal Halide Perovskites as Visible-Light Sensitizers for Photovoltaic Cells. *J. Am. Chem. Soc.* **2009**, *131*, 6050−6051.

(3) NREL. http://www.nrel.gov/ncpv/images/efficiency_chart.jpg (accessed 2014).

(4) Matteocci, F.; Cinà, L.; Di Giacomo, F.; Razza, S.; Palma, A. L.; Guidobaldi, A.; D'Epifanio, A.; Licoccia, S.; Brown, T. M.; Reale, A.; Di Carlo, A. High Efficiency Photovoltaic Module Based on Mesoscopic Organometal Halide Perovskite. *Prog. Photovoltaics* **2014**, DOI: 10.1002/pip.2557.

(5) Razza, S.; Di Giacomo, F.; Matteocci, F.; Cinà, L.; Palma, A. L.; Casaluci, S.; Cameron, P.; D'Epifanio, A.; Licoccia, S.; Reale, A.; Brown, T. M.; Di Carlo, A. Perovskite Solar Cells and Large Area Modules (100 cm^2) Based on an Air Flow-assisted PbI_2 Blade Coating Deposition Process. *J. Power Sources* **2015**, *277*, 286−291.

(6) Yang, J.; Siempelkamp, B. D.; Liu, D.; Kelly, T. L. Investigation of CH3NH3PbI3 Degradation Rates and Mechanisms in Controlled Humidity Environments Using in Situ Techniques. *ACS Nano* **2015**, *9*, 1955−1963.

(7) Noh, J. H.; Im, S. H.; Heo, J. H.; Mandal, T. N.; Seok, S. I. Chemical Management for Colorful, Efficient, and Stable Inorganic−Organic Hybrid Nanostructured Solar Cells. *Nano Lett.* **2013**, *13*, 1764−1769.

(8) Niu, G.; Li, W.; Meng, F.; Wang, L.; Dong, H.; Qiu, Y. Study on the Stability of CH3NH3PbI3 Films and the Effect of Post-modification by Aluminum Oxide in All-solid-state Hybrid Solar Cells. *J. Mater. Chem. A* **2014**, *2*, 705−710.

(9) Guarnera, S.; Abate, A.; Zhang, W.; Foster, J. M.; Richardson, G.; Petrozza, A.; Snaith, H. J. Improving the Long-Term Stability of Perovskite Solar Cells with a Porous Al2O3 Buffer Layer. *J. Phys. Chem. Lett.* **2015**, *6*, 432−437.

(10) You, J.; Yang, Y.; Hong, Z.; Song, T. B.; Meng, L.; Liu, Y.; Jiang, C.; Zhou, H.; Chang, W. H.; Li, G.; Yang, Y. Moisture Assisted Perovskite Film Growth for High Performance Solar Cells. *Appl. Phys. Lett.* **2014**, *105*, 183902.

(11) Han, Y.; Meyer, S.; Dkhissi, Y.; Weber, K.; Pringle, J. M.; Bach, U.; Spiccia, L.; Cheng, Y. B. Degradation Observations of Encapsulated Planar CH3NH3PbI3 Perovskite Solar Cells at High Temperatures and Humidity. *J. Mater. Chem. A* **2015**, *3*, 8139−8147.

(12) Matteocci, F.; Razza, S.; Di Giacomo, F.; Casaluci, S.; Mincuzzi, G.; Brown, T. M.; D'Epifanio, A.; Licoccia, S.; Di Carlo, A. Solid-state Solar Modules Based on Mesoscopic Organometal Halide Perovskite: A Route Towards the Up-scaling Process. *Phys. Chem. Chem. Phys.* **2014**, *16*, 3918−3923.

(13) Burschka, J.; Pellet, N.; Moon, S. J.; Baker, R. H.; Gao, P.; Nazeeruddin, M. K.; Gratzel, M. Sequential Deposition as a Route to High-performance Perovskite-sensitized Solar Cells. *Nature* **2013**, *499*, 316−319.

(14) Kim, H. S.; Park, N. G. Parameters Affecting I−V Hysteresis of CH3NH3PbI3 Perovskite Solar Cells: Effects of Perovskite Crystal Size and Mesoporous TiO2 Layer. *J. Phys. Chem. Lett.* **2014**, *5*, 2927−2934.

(15) Di Giacomo, F.; Razza, S.; Matteocci, F.; D'Epifanio, A.; Licoccia, S.; Brown, T. M.; Di Carlo, A. High Efficiency $CH_3NH_3PbI_{(3-x)}Cl_x$ Perovskite Solar Cells with Poly(3-hexylthiophene) Hole Transport Layer. *J. Power Sources* **2014**, *251*, 152−156.

(16) Yantara, N.; Yanan, F.; Shi, C.; Dewi, H. A.; Boix, P. P.; Mhaisalkar, S. G.; Mathews, N. Unravelling the Effects of Cl Addition in Single Step CH3NH3PbI3. *Chem. Mater.* **2015**, *27*, 2309−2314.
(17) Chen, Q.; Zhou, H.; Hong, Z.; Luo, S.; Duan, H. S.; Wang, H. H.; Liu, Y.; Li, G.; Yang, Y. Planar Heterojunction Perovskite Solar Cells via Vapor-Assisted Solution Process. *J. Am. Chem. Soc.* **2014**, *136*, 622−625.
(18) Casaluci, S.; Cinà, L.; Pockett, A.; Kubiak, P. S.; Niemann, R. G.; Reale, A.; Di Carlo, A.; Cameron, P. J. A simple approach for the fabrication of perovskite solar cells in air. *J. Power Sources* **2015**, *297*, 504−510.
(19) Jeon, N. J.; Noh, J. H.; Kim, Y. C.; Yang, W. S.; Ryu, S. C.; Seok, S. I. Compositional Engineering of Perovskite Materials for High-performance Solar Cells. *Nat. Mater.* **2014**, *13*, 897−903.
(20) Zhou, H.; Chen, Q.; Li, G.; Luo, S.; Song, T. B.; Duan, H. S.; Hong, Z.; You, J.; Liu, Y.; Yang, Y. Interface Engineering of Highly Efficient Perovskite Solar Cells. *Science* **2014**, *345*, 542−546.
(21) Im, J. H.; Kim, H. S.; Park, N. G. Morphology-photovoltaic Property Correlation in Perovskite solar cells: One-step versus Two-step Deposition of CH3NH3PbI3. *APL Mater.* **2014**, *2*, 081510.
(22) Yantara, N.; Sabba, D.; Yanan, F.; Kadro, J. M.; Moehl, T.; Boix, P. P.; Mhaisalkar, S.; Graetzel, M.; Graetzel, C. Loading of Mesosporous Titania films by CH3NH3PbI3 Perovskite, Single step vs Sequential deposition. *Chem. Commun.* **2015**, *51*, 4603−4606.
(23) Laban, W. A.; Etgar, L. Depleted hole conductor-free lead halide iodide heterojunction solar cell. *Energy Environ. Sci.* **2013**, *6*, 3249−3253.
(24) Ko, H. S.; Lee, J. W.; Park, N. G. 15.76% Efficiency Perovskite Solar Cell Prepared under High Relative Humidity: Importance of PbI2Morphology in Two-Step Deposition of CH3NH3PbI3. *J. Mater. Chem. A* **2015**, *3*, 8808−8815.
(25) Wehbe, N.; Pireaux, J. J.; Houssiau, L. XPS Evidence for Negative Ion Formation in SIMS Depth Profiling of Organic Material with Cesium. *J. Phys. Chem. C* **2014**, *118*, 26613−26620.
(26) Cappel, U. B.; Daeneke, T.; Bach, U. Oxygen-Induced Doping of Spiro-MeOTAD in Solid-State Dye-Sensitized Solar Cells and Its Impact on Device Performance. *Nano Lett.* **2012**, *12*, 4925−4931.
(27) Philippe, B.; Park, B. W.; Lindblad, R.; Oscarsson, J.; Ahmadi, S.; Johansson, E. M. J.; Rensmo, H. Chemical and Electronic Structure Characterization of Lead Halide Perovskites and Stability Behavior under Different Exposures- A Photoelectron Spectroscopy Investigation. *Chem. Mater.* **2015**, *27*, 1720−1731.
(28) Starr, D. E.; Sadoughi, G.; Handick, E.; Wilks, R. G.; Alsmeier, J. H.; Köhler, L.; Gorgoi, M.; Snaith, H. J.; Bärace, M. Direct observation of an inhomogeneous chlorine distribution in CH3NH3PbI3−xClx layers: surface depletion and interface enrichment. *Energy Environ. Sci.* **2015**, *8*, 1609−1615.
(29) Busby, Y.; Crespo-Monteiro, N.; Girleanu, M.; Brinkmann, M.; Ersen, O.; Pireaux, J. J. 3D Imaging of Filaments in Organic Resistive Memory Devices. *Org. Electron.* **2015**, *16*, 40−45.
(30) Casula, G.; Cosseddu, P.; Busby, Y.; Pireaux, J. J.; Rosowski, M.; Tkacz Szczesna, B.; Soliwoda, K.; Celichowski, G.; Grobelny, J.; Novák, J.; Banerjee, R.; Schreiber, F.; Bonfiglio, A. Air-stable, Non-volatile Resistive Memory Based on Hybrid Organic/Inorganic Nanocomposites. *Org. Electron.* **2015**, *18*, 17−23.
(31) Matteocci, F.; Mincuzzi, G.; Giordano, F.; Capasso, A.; Artuso, E.; Barolo, C.; Viscardi, G.; Brown, T. M.; Reale, A.; Di Carlo, A. Blocking Layer Optimisation of Poly(3-hexylthiopene) Based Solid State Dye Sensitized Solar Cells. *Org. Electron.* **2013**, *14*, 1882−1890.
(32) Langford, R. M.; Rogers, M. In situ lift-out: Steps to improve yield and a comparison with other FIB TEM sample preparation techniques. *Micron* **2008**, *39*, 1325−1330.

DOI: 10.1021/acsami.5b08038
ACS Appl. Mater. Interfaces 2015, 7, 26176−26183